JOURNAL OF SPACECRAFT AND ROCKETS
Vol. 44, No. 6, November–December 2007

Density and Winds in the Thermosphere Deduced from Accelerometer Data

Eric K. Sutton,* R. Steven Nerem,† and Jeffrey M. Forbes†
University of Colorado, Boulder, Colorado 80309

DOI: 10.2514/1.28641

With the emergence and increased use of highly accurate accelerometers for geodetic satellite missions, a new opportunity has arisen to study nonconservative forces acting on a number of satellites with high temporal resolution. As the number of these satellite missions increases, so does our ability to determine the spatial characteristics and time response of total density and winds in the thermosphere. This paper focuses on the derivation and methodology of inferring density and winds from along-track and cross-track accelerometer measurements, with the main goal of determining the feasibility of this data set. The principal sources of error such as solar radiation pressure, the unknown coefficients of drag and lift, instrument precision and biases, and unaccounted-for winds are discussed in the context of both density and winds. In the context of our treatment of errors, density errors are generally less than 15%, whereas wind-speed errors are more substantial. Finally, comparisons of results to existing empirical models (i.e., horizontal wind model 93) and to self-consistent numerical models (i.e., thermosphere–ionosphere electrodynamic general circulation model) are provided. Comparisons of results to ion drift velocities (as measured by Defense Meteorological Satellite Program) are also provided.

Nomenclature

A	=	satellite panel area, m^2
$\boldsymbol{a}$	=	acceleration, m/s^2
C_D	=	coefficient of drag
C_L	=	coefficient of lift
m	=	satellite mass, kg
$\hat{n}$	=	satellite panel unit vector
$\boldsymbol{v}$	=	satellite velocity, m/s
$\boldsymbol{w}$	=	wind velocity, m/s
θ	=	angle of incidence
ρ	=	atmospheric density (calculated from the challenging minisatellite payload), kg/m^3

Subscripts

c	=	relative to a corotating atmosphere
d	=	drag
dl	=	drag and lift
ea	=	Earth albedo
i	=	satellite panel number
ir	=	infrared radiation
l	=	lift
sr	=	solar radiation
x	=	along-track accelerometer axis
y	=	cross-track accelerometer axis
z	=	radial accelerometer axis

I. Introduction

IN THE past 10 years, the thermosphere community has called for a movement from station-based and regional studies to global studies spanning several decades [1–3]. Since these recommendations were made, there have been several additions to the ionospheric and thermospheric measurement community, such as mapping of O/N_2 ratios and total electron content measurements from global position system (GPS) constellation satellites. A complementing technology is the use of satellite accelerometers to provide in situ estimates of neutral density and wind.

As more satellite missions are beginning to use high-accuracy accelerometers such as the Challenging Minisatellite Payload [4] (CHAMP), which was launched in 2000, the Gravity Recovery and Climate Experiment [5] (GRACE), which was launched in 2001, the Gravity Field and Steady-state Ocean Circulation Explorer [6] (GOCE), with launch scheduled for 2007, and Swarm [7], with launch scheduled for 2009, the coverage is becoming more global. CHAMP and GRACE missions alone cover four local times at all latitudes, with temporal sampling of 0.1 and 1 Hz, respectively. The increased use of accelerometers is due partly to an increase in the instrument's sensitivity. The sensitivity of the accelerometer instruments has increased by several factors of 10 in the last decade alone, making them suitable for use at higher altitudes in which there is less drag force [4,8]. These issues are beneficial to the thermosphere community, providing not only an increase in accuracy, but also longer mission lifetimes for long-term studies. Because the purpose for these accelerometers is usually focused on gravity recovery and other geodetic studies, data can be acquired at little or no cost to the thermosphere community.

Although retrieving global data is a step in the right direction, it is only half of the battle. Many of the beneficiaries of space weather forecasts (such as civil, commercial, and government-run satellite missions) need to predict conditions to accurately calculate satellite ephemeris. In terms of a broader scale, all systems that are affected by the thermosphere greatly benefit from accurate predictions, whether the system is the magnetosphere, the mesosphere, or even large-scale power grids. Many have attempted to model and predict thermospheric density and temperature, such as the Jacchia model series [9], the mass spectrometry and incoherent scatter (MSIS) model series [10] and the drag-temperature model (DTM) series [11]. However, there is still a large bias in these models, combined with a poor spatial resolution and problems caused by a lack of integration of the true physical processes occurring and lack of a complete set of thermosphere measurements that thoroughly represents the dynamics of the system.

Ideally, it would be possible to quantitatively predict the global state of the thermosphere a number of days in advance. The ability to accurately predict implies understanding of the physical mechanisms at work in the system. The thermosphere is a dynamic and multiconstituent system coupled to the mesosphere at the lower

Presented as Paper 6170 at the AIAA/AAS Astrodynamics Specialist Conference and Exhibit, Keystone, CO, 21–24 August 2006; received 31 October 2006; accepted for publication 10 May 2007.

*Ph.D. Candidate, Aerospace Engineering Sciences, Campus Box 429.
†Professor, Aerospace Engineering Sciences, Campus Box 429.

boundary through turbulent mixing and the propagation and dissipation of gravity waves and tides, the magnetosphere at the upper boundary through particle precipitation and convection electric fields, and directly to the sun through solar radiation absorption by thermospheric constituents [8]. A thorough understanding of this system cannot be realized without the appropriate combination of measurements. The increased use of highly accurate accelerometers provides an opportunity to study the thermosphere with unprecedented spatial and temporal resolution.

The main purpose of this paper is to establish and validate the methodology necessary to infer neutral density and wind speeds from satellite accelerometer data. Section II gives a detailed explanation of the processing of data. Section III uses the methodology outlined in Sec. II to estimate the errors that should be expected from the neutral density and wind calculations. Assuming that these methods can be validated, the secondary goal of this paper is to highlight the numerous applications of this data set within the thermosphere measurement community. Two examples of the possible applications for this data set are given in Sec. IV.

II. Data Processing

Onboard the CHAMP satellite is the STAR accelerometer, which measures the sum of all forces on the satellite's surface. This measured quantity is mostly composed of the force imparted to the satellite by atmospheric drag, with lesser constituents such as atmospheric lift and solar and Earth radiation pressure also contributing. By modeling the effects of solar and Earth radiation pressure, we obtain a method of isolating the acceleration caused by atmospheric drag and lift. These modeled accelerations can be subtracted from the total nongravitational forces, as measured by the accelerometer.

CHAMP data were provided for our use by the CHAMP Information System and Data Center (ISDC).[‡] Acceleration, attitude, and orbit-ephemeris data files were used in the calculations pertaining to this study. The acceleration and attitude data are provided on a 10-s interval, which is processed from the original 1-Hz data to remove acceleration spikes caused by spacecraft maneuvers. Accelerations in both the along-track direction and the cross-track direction are thought to be accurate to 3×10^{-9} ms^{-2} [12]. Accelerations in the radial direction are not used in these studies, because they are less sensitive by a factor of 10 and have had repeated troubles since launch [12].

The following sections explain the finer details of processing density and winds from accelerometer measurements from the CHAMP satellite. These methods can be readily applied to other missions such as GRACE. In Sec. II.A, density calculations are made assuming that we have a measurement for the acceleration caused only by atmospheric drag and lift. Again in Sec. II.B, the same assumption is made to estimate wind speed. In truth, the measurements available are corrupted by solar radiation pressure (SRP) and Earth radiation pressure. Section II.C describes the ways in which these forces are modeled and subtracted from the accelerometer measurements before density calculations are performed. The remaining sections discuss estimation of accelerometer instrument biases, coefficients of drag and lift, and their impact on calculations of density and wind.

A. Total Mass Density

If we break down the satellite into a macromodel of 13 individual flat plates [13], we can express the acceleration caused by the drag and lift forces imparted to each plate by Eqs. (1a) and (1b), respectively:

$$a_d = -\tfrac{1}{2}(C_D A/m)\rho|\boldsymbol{v}|^2 \tag{1a}$$

$$a_l = -\tfrac{1}{2}(C_L A/m)\rho|\boldsymbol{v}|^2 \tag{1b}$$

[‡]Data available at http://isdc.gfz-potsdam.de/ [retrieved 25 May 2006].

where a_d is the acceleration caused by drag acting in the direction of $\boldsymbol{v}$, a_l is the acceleration caused by lift acting in the direction of $(\boldsymbol{v} \times \hat{n}) \times \boldsymbol{v}$, $\hat{n}$ is the unit normal vector to the satellite plate, C_D is the coefficient of drag, C_L is the coefficient of lift, A is the total plate area, m is the satellite mass, and $\boldsymbol{v}$ is the velocity of the satellite with respect to the surrounding atmosphere. We can then separate $\boldsymbol{v}$ into two components: the velocity of the satellite with respect to an atmosphere that corotates with the Earth, $\boldsymbol{v}_c$, and the velocity of any deviation in wind speed, $\boldsymbol{w}_c$. In other words, $\boldsymbol{v}$ was separated such that $\boldsymbol{v} = \boldsymbol{v}_c - \boldsymbol{w}_c$. We can sum the effects of each plate from the satellite macromodel and express the total acceleration caused by drag and lift in vector form:

$$\boldsymbol{a}_{\mathrm{dl}} = -\frac{\rho}{2m}\sum_{i=1}^{13}\Big\{A_i C_{Di}[(\boldsymbol{v}_c - \boldsymbol{w})\cdot\hat{n}_i](\boldsymbol{v}_c - \boldsymbol{w}) + A_i\frac{\cos\theta_i}{\sin\theta_i}C_{Li}[(\boldsymbol{v}_c - \boldsymbol{w})\times\hat{n}_i]\times(\boldsymbol{v}_c - \boldsymbol{w})\Big\} \tag{2}$$

where $\boldsymbol{a}_{\mathrm{dl}}$ is the acceleration caused by drag and lift, A_i is the plate area, C_{Di} is the coefficient of drag for the plate, C_{Li} is the coefficient of lift for the plate, m is the satellite mass, $\hat{n}_i$ is the unit plate normal, ρ is the atmospheric density, $\boldsymbol{v}_c$ is the satellite velocity relative to a corotating atmosphere, and θ is the angle between $\hat{n}_i$ and $\boldsymbol{v}$. This equation can then be solved for the density and cross-track wind in terms of the acceleration measured by the satellite.

When estimating density, the wind relative to a corotating atmosphere, $\boldsymbol{w}_c$, is assumed to be negligible. This is done out of necessity, and the errors incurred by this assumption are discussed in Sec. III.A. With this assumption, Eq. (2) is solved for density using the along-track axis of the accelerometer denoted by $\boldsymbol{a}_{\mathrm{dl}}\cdot\hat{x}$, giving Eq. (3):

$$\rho = \frac{-2m(\boldsymbol{a}_{\mathrm{dl}}\cdot\hat{x})}{\sum_{i=1}^{13}\{A_i C_{Di}[\boldsymbol{v}_c\cdot\hat{n}_i]\boldsymbol{v}_c + A_i(\cos\theta_i/\sin\theta_i)C_{Li}[\boldsymbol{v}_c\times\hat{n}_i]\times\boldsymbol{v}_c\}\cdot\hat{x}} \tag{3}$$

where ρ is the atmospheric density calculated from CHAMP/STAR, and $\hat{x}$ is the unit vector in the along-track direction.

B. Cross-Track Wind Speed

It is also possible to obtain an estimate of the neutral wind vector component in the direction of the cross-track axis of the STAR accelerometer. The steps for this calculation are similar to those for density calculations using Eq. (2). This derivation is slightly more involved, because we are solving for $\boldsymbol{w}_c$ instead of ρ. Only the cross-track axis is studied here for the following two reasons: neutral density and wind speed cannot be separated from each other in calculations using the along-track accelerometer axis (there are two unknowns and only one equation), and the radial accelerometer axis does not provide measurements of sufficient accuracy. Thus, when solving Eq. (2) for wind speed, components of $\boldsymbol{w}_c$ in the along-track and radial directions are assumed to be zero. Just as in Sec. II.A, this is done out of necessity, and the resulting error is discussed in Sec. III.A. The density term in Eq. (2) is now the neutral density derived from the along-track accelerometer axis.

This paper compares two independent solutions to Eq. (2) to assess the error incurred by each method. In both solutions, the vector equation is broken into three scalar equations for acceleration in the along-track, cross-track, and radial directions. The first solution, the single-axis method, uses only the cross-track scalar equation to solve for cross-track wind. This solution takes the form of a quadratic equation and must be treated accordingly. The second solution, the dual-axis method, makes use of a substitution between the along-track and cross-track scalar equations. This method is an adaptation of the solution given by Liu et al. [14]. Although both methods use the same underlying assumptions, the main difference is in the manipulation of the lift term of Eq. (2). The single-axis method solves the cross-track component of Eq. (2) directly for the cross-track component of $\boldsymbol{w}_c$. On the other hand, the dual-axis method

subtracts the lift term from Eq. (2) and uses the along-track and the cross-track components of Eq. (2) to solve for the cross-track component of $\boldsymbol{w}$. The dual-axis method yields a less complex equation that has cancelled out some of the terms that cause error. Both solutions have advantages and disadvantages in the context of error propagation, which are discussed in Sec. III. For the derivation of these two approaches, see the Appendix.

C. Modeling Nonconservative Forces

Modeling nonconservative forces, aside from atmospheric drag, is an important step in density and wind calculations. Accelerometers measure any acceleration of a satellite that is not caused by gravity. Although the largest component of this measurement in the thermosphere is caused by atmospheric drag, according to our models, up to 10% can be caused by other sources. SRP is the largest of these, followed by albedo and infrared radiation from Earth. To accurately infer density and wind speed, these forces must be subtracted from the original accelerometer measurements. The next few subsections deal with modeling these forces.

1. Solar Radiation Pressure

Much like Eq. (2), the SRP model employs a 13-plate macromodel of the satellite. When the satellite is sunlit, attitude quaternions are used to calculate the angle between the satellite–sun vector and the normal vector for each plate that is facing the sun. The following equation can then be used to determine the entire resultant force on the satellite due to solar radiation [15]:

$$\boldsymbol{a}_{\mathrm{sr}} = \sum_{i=1}^{13} -\frac{RA_i \cos(\phi_{\mathrm{inc},i})}{mc}\left[2\left(\frac{c_{\mathrm{rd},i}}{3} + c_{\mathrm{rs},i}\cos(\phi_{\mathrm{inc},i})\right)\hat{n}_i + (1 - c_{\mathrm{rs},i})\hat{s}\right] \tag{4}$$

where $\boldsymbol{a}_{\mathrm{sr}}$ is the acceleration caused by SRP, A_i is the plate area, c is the speed of light, $c_{\mathrm{rd},i}$ is the coefficient of diffusive reflectivity, $c_{\mathrm{rs},i}$ is the coefficient of specular reflectivity, m is the satellite mass, $\hat{n}_i$ is the unit plate normal, $\phi_{\mathrm{inc},i}$ is the angle of incidence of the sun with respect to the plate, R is the flux originating from the sun, and $\hat{s}$ is the unit satellite–sun vector. The magnitude of solar flux is also multiplied by a ratio to account for shadowing when the satellite is in the umbra or penumbra shadow regions. The modifying ratio is equivalent to the percentage of the sun visible by the satellite. Finding the sun–Earth vector and the appropriate flux acting on the satellite requires up-to-date Jet Propulsion Laboratory solar and planetary ephemerides (version DE-405). Typical along-track magnitudes for this term are on the order of 3×10^{-8} ms^{-2}.

As a validation of this method, jumps in measured acceleration as the satellite enters and leaves the Earth's shadow were studied. When the along-track accelerometer axis aligns with the satellite–sun vector (i.e., near noon/midnight local times), the jumps in acceleration can be related to the modeled accelerations with a high level of precision. During 2003, an approximate ratio of modeled SRP to measured SRP was found to be 0.86 ± 0.08. Deviation of this ratio from 1 indicates an error in modeling SRP likely caused by an error in the coefficients of reflectivity (given in Table 1). This ratio was applied to measurements from the cross-track direction to correct wind-speed data.

2. Albedo and Infrared Radiation Pressures

The albedo calculations require a latitudinally varying model for shortwave radiation (in terms of albedo) and longwave radiation (in terms of emissivity) coming from the terrestrial sphere. The effect of the Earth is summed by using discrete elements according to Knocke et al. [16]. The following equation can be used to sum the effect of each Earth element on each satellite plate:

$$\boldsymbol{a}_{\mathrm{ea}} = \sum_{i=1}^{13}\sum_{j} -\frac{R_j A_i \cos(\phi_{\mathrm{inc},ij})}{mc}\left[2\left(\frac{c_{\mathrm{rd},i}}{3} + c_{\mathrm{rs},i}\cos(\phi_{\mathrm{inc},ij})\right)\hat{n}_i + (1 - c_{\mathrm{rs},i})\hat{s}_j\right] \tag{5}$$

where $\boldsymbol{a}_{\mathrm{ea}}$ is the acceleration caused by Earth radiation pressure, A_i is the plate area, c is the speed of light, $c_{\mathrm{rd},i}$ is the coefficient of diffusive reflectivity, $c_{\mathrm{rs},i}$ is the coefficient of specular reflectivity, m is the satellite mass, $\hat{n}_i$ is the unit plate normal, $\phi_{\mathrm{inc},ij}$ is the angle of incidence of the source with respect to the plate, R_j is the flux originating from the source j, and $\hat{s}_j$ is the unit satellite-source vector. Approximately 168 Earth elements are required for this summation at the height of the CHAMP satellite. Both the SRP model and the albedo/infrared models were adapted from the Geodyn 2 orbit determination software package (NASA Goddard Space Flight Center). Typical along-track magnitudes for this term are on the order of 5×10^{-10} and 2×10^{-10} ms^{-2} for albedo and infrared radiation pressures, respectively.

3. Satellite Properties

The last pieces of information needed to accurately model surface forces caused by radiation are the geometry and physical properties of the satellite. These parameters were measured by Daimler–Benz Aerospace before launch [17]. The satellite is divided into 13 segments, each assumed to be a flat plate. Measurements of normal unit vectors, area, diffuse and specular reflectivities (for longwave and shortwave radiation), and types of materials for each plate are listed in Table 1 [13].

D. Instrument Calibration

An electrostatic accelerometer onboard a satellite measures the amount of voltage it takes to maintain a proof mass in a certain position in reference to the satellite. To know accurately and precisely what the force is, the linear relationship between force and voltage must be known. With most instruments, there is a drift in this linear relationship, depending on many different factors. In the case of CHAMP, drift is mainly caused by temperature fluctuations. To

Table 1 CHAMP surface properties

Panel	Area, m^2	c_{rs}, visible	c_{rd}, visible	c_{rs}, infrared	c_{rd}, infrared	Material
Top	1.2920	0.05	0.30	0.03	0.16	SiO_2
Bottom	3.6239	0.68	0.20	0.19	0.06	Teflon
Left	3.1593	0.05	0.30	0.03	0.16	SiO_2
Left (rear)	0.3020	0.40	0.26	0.23	0.15	Kapton/SiO_2
Right	3.1593	0.05	0.30	0.03	0.16	SiO_2
Right (rear)	0.3020	0.40	0.26	0.23	0.15	Kapton/SiO_2
Aft	0.4902	0.40	0.26	0.23	0.15	Kapton/SiO_2
Front	1.2199	0.20	0.40	0.26	0.51	Sandblasted Al
Boom (top)	0.9300	0.40	0.26	0.23	0.15	Kapton/SiO_2
Boom (bottom)	0.9300	0.40	0.26	0.23	0.15	Kapton/SiO_2
Boom (left)	0.9300	0.40	0.26	0.23	0.15	Kapton/SiO_2
Boom (right)	0.9300	0.40	0.26	0.23	0.15	Kapton/SiO_2
Front	0.0529	0.20	0.40	0.26	0.51	Sandblasted Al

have the most accurate density calculations, a bias and scale factor must be estimated and applied to the raw acceleration data.

For this study, a least-squares method was used to estimate the bias factors for the along-track accelerometer axes. With this method, the bias factors are estimated on a daily basis using the STAR accelerometer measurements as an orbit determination force model, while letting the estimated orbit converge on the orbit ephemeris provided by the CHAMP ISDC. The along-track a priori bias factor used in our estimating scheme is -2.925×10^{-6} ms^{-2}. The rms of the bias factors after detrending is 6.465×10^{-9} ms^{-2}. In this process, biases are considered to be inaccurate when they differ from the mean by more than 2.260×10^{-8} ms^{-2}. When the numbers lie outside of this range, linear interpolation is used.

For the cross-track axis, bias and scale factors are estimated on a daily basis, assuming that on average, low-latitude winds agree with a corotating atmosphere. This is done because our orbit determination method is less sensitive to accelerations in the cross-track and radial axes. Using this method makes the wind database systematically biased, as will be shown in Sec. III.A. The rms of the bias factors after detrending is 5.176×10^{-9} ms^{-2}, whereas the rms of the scale factors after detrending is 0.0188.

E. Coefficients of Drag and Lift

The final unknown in this process is the coefficient of drag for each plate of the CHAMP macromodel [see Eq. (2)]. Generally, these coefficients are estimated using precise orbit determination in terms of a neutral density model. However, for this application, we desire that the coefficient of drag not exhibit the same biases inherent in the corresponding neutral density model. Therefore, a physics-based model for approximating the coefficient of drag for a flat plate was used. This method, outlined by Cook [18], leads to the following formulas for drag and lift:

$$C_{Di} = 2\left[1 + \frac{2}{3}\sqrt{1 + \alpha_i\left(\frac{T_{w,i}}{T_a} - 1\right)}\cos(\theta_i)\right] \tag{6a}$$

$$C_{Li} = \frac{4}{3}\sqrt{1 + \alpha_i\left(\frac{T_{w,i}}{T_a} - 1\right)}\sin(\theta_i) \tag{6b}$$

where C_{Di} is the coefficient of drag, C_{Li} is the coefficient of drag, α_i is the accommodation coefficient, T_a is the temperature of the atmosphere, $T_{w,i}$ is the temperature of the plate, and θ_i is the angle of incident gas flow with respect to the plate. Further, readmittance of atmospheric molecules is assumed to be diffusive because the temperature of the satellite is relatively cool (assumed to be 273.0 K after Bruinsma and Biancale, 2003 [17]). This assumption leads to the following approximation for the accommodation coefficient that appears in Eqs. (6a) and (6b):

$$\alpha_i = \frac{3.6\mu_i}{(1 + \mu_i)^2} \tag{7}$$

where μ_i is the ratio of mass of the incident gas atom to the mass of the surface atom. The acceleration caused by impacting and readmitting atoms and molecules can be represented by Eq. (2) in terms of the coefficient of drag C_{Di} and the coefficient of lift C_{Li}.

When using accelerometer data from a long satellite, such as CHAMP, Eqs. (6a), (6b), and (7) are believed to lead to a systematic underestimation of the coefficient of drag. This is caused by the fact that a large area of the satellite is exposed to the airstream at grazing incidence [19].

III. Error Analysis

For a linear calculation based on n independent variables $x_1, x_2, \cdots, x_n$, the uncertainties propagate through to the dependent variable $y(x_1, x_2, \cdots, x_n)$ in the following way:

$$u_y = \sqrt{\left(\frac{\partial y}{\partial x_1}u_{x_1}\right)^2 + \left(\frac{\partial y}{\partial x_2}u_{x_2}\right)^2 + \cdots + \left(\frac{\partial y}{\partial x_n}u_{x_n}\right)^2} \tag{8}$$

where $u_{x_1}, u_{x_2}, \cdots, u_{x_n}$ are the uncertainties of the n independent variables. For a nonlinear function involving $x_1, x_2, \cdots, x_n$, Eq. (8) becomes a first-order approximation of the uncertainty in y. It is common practice to assume that the uncertainties are small enough for this approximation to remain realistic [20]. Both systematic and random (noise) errors are valid inputs into this equation.

In the following error budget, Eq. (8) was applied to Eq. (3) for density and the two solutions to Eq. (2) for wind calculations (see the Appendix). In turn, the error can be calculated for each data point of density and wind, making it possible to complete a long-term error analysis. One orbit, starting at 0324 hrs Universal Time (UT) on day 300 of 2003 is used to illustrate the typical error sources in both density and wind estimates.

In the following sections, the sources of error were separated into the two categories of systematic and noise errors. The main constituents of systematic error are the estimated bias and scale factors that are applied to the along-track and cross-track accelerometers, the underestimated coefficients of drag and lift, and winds that are assumed to be zero during the calculations of density and cross-track wind speed. Noise error is caused mostly by the precision of the accelerometer and inaccuracies in the SRP model.

A. Systematic Error Sources

1. *Instrument Calibration*

Calibration factors are estimated for each day of data, therefore, any resulting errors in density and wind data will appear to be systematic over the course of one day but random over a longer period of time. Figure 1 shows the error in density calculations caused by errors in bias and scale factors. For this orbit, an error of 0.0188 in the scale factor and an error of 6.465×10^{-9} ms^{-2} in the bias factor (see Sec. II.D) lead to a mean error of 4.4% in density. Because of the changing satellite trajectory and attitude during this orbit, the error can be as high as 9.5%.

Figure 2 shows the large effect of instrument calibration on wind estimates using both solutions to Eq. (2). An error of 0.0188 in the along-track scale factor and an error of 6.465×10^{-9} ms^{-2} in the along-track bias factor lead to a mean error of 51.4 and 46.7 ms^{-1} when using the single-axis and dual-axis methods, respectively.

For cross-track wind calculations, the additional calibration of the cross-track accelerometer axis is required (see Sec. II.D). An error of 0.0188 in the cross-track scale factor and an error of 5.176×10^{-9} ms^{-2} in the cross-track bias factor lead to a mean error of 97.2 and 95.8 ms^{-1} when using the single-axis and dual-axis methods, respectively.

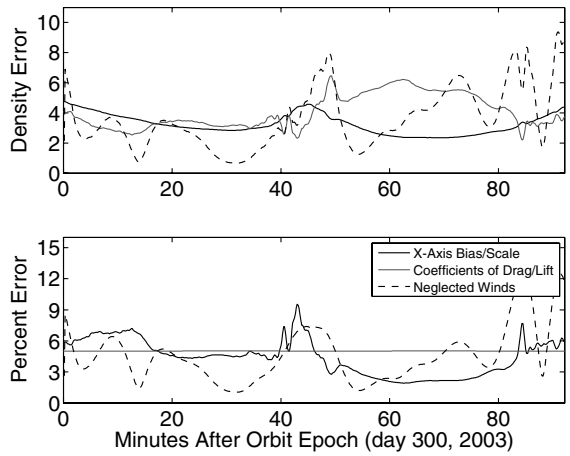

Fig. 1 Systematic error (top, 10^{-13} kg/m^3) and percent error (bottom) in density estimates.

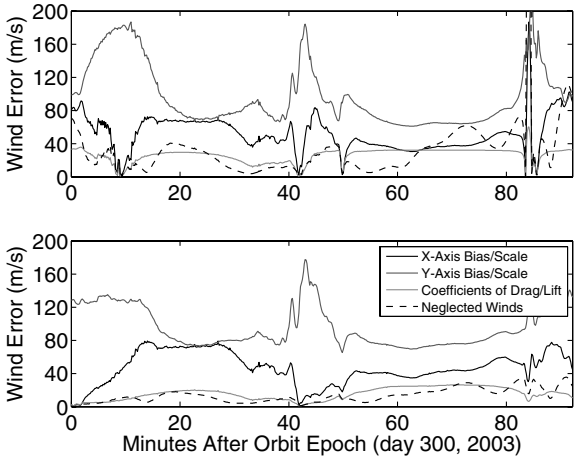

Fig. 2 Systematic error in wind estimates when using the single-axis method (top) and the dual-axis method (bottom).

2. Coefficients of Drag and Lift

Figure 1 also shows the error in density calculations caused by errors in the coefficients of drag and lift. A systematic error of 5% in both coefficients was assumed. Although errors caused by lift are extremely small, on the order of 0.02%, errors caused by drag constitute a fairly constant 5.0% error in density calculations.

The amount of error contributed by the coefficients of drag and lift when using the single-axis method can be seen in the top panel of Fig. 2. Generally, this error has a mean of 26.0 ms^{-1}. However, due to the complexity of the single-axis solution, at times there are larger spikes in error, as seen in Fig. 2 around 84 min.. These spikes can also be seen in the cross-track wind-speed estimates; however, spikes in error are usually more pronounced, due to the linearization process of Eq. (8). At certain times, due to satellite attitude and trajectory, this linearization becomes very sensitive to any errors in the coefficients of drag and lift. This particular orbit was chosen to illustrate this limitation for the single-axis method.

The bottom panel of Fig. 2 shows the fairly small amounts of error caused by the coefficients of drag and lift using the dual-axis method, never exceeding 26.3 ms^{-1}. The spikes seen when using the single-axis method no longer exist, and the errors are much smaller and more stable in general. With the dual-axis method, the propagation of errors caused by the coefficient of drag is severely reduced, due to a substitution of terms (see the Appendix). For this orbit, mean wind-speed errors caused by the coefficients of drag and lift are 15.4 ms^{-1}.

Including lift into calculations of wind speed is extremely important. Figure 3 shows wind speed calculated twice using the dual-axis method, once accounting for lift and once neglecting it, as is done in Liu et al. [14]. The absolute difference between the two methods, seen in Fig. 3, is on the order of 100–500 ms^{-1}. This difference can become even larger at times, as well as very small, depending on satellite attitude and trajectory.

3. Neglected Wind Speed

Wind speeds in the along-track, cross-track, and radial directions are assumed to be equal to zero when making density calculations. Using the horizontal wind model (HWM-93), we were able to simulate the error incurred during this process caused by any neglected along-track $w_{c,x}$ and cross-track $w_{c,y}$ winds. For the radial direction $w_{c,z}$, we used a constant error of 5 ms^{-1}. Figure 1 shows the error in density estimates caused by neglecting along-track, cross-track, and radial wind speeds. Near the poles, unaccounted-for winds can become the largest systematic error source, with a mean error of 4.6%. As the winds increase near the poles, there is a maximum of 12.6% error in density.

Errors in cross-track wind speeds, using both solutions to Eq. (2), caused by the neglect of winds in the along-track, cross-track [propagating from the along-track density estimates used in Eqs. (A5e) and (A8b)], and radial directions can be seen in Fig. 2. Although the propagation of most error sources are comparable when using either solution to Eq. (2), the dual-axis method performs much better in the context of the neglected winds. For this orbit, the mean wind-speed errors are 31.56 and 13.29 ms^{-1} when using the single-axis and dual-axis methods, respectively. In addition, there are spikes in error seen when using the single-axis method, which do not occur when using the dual-axis method.

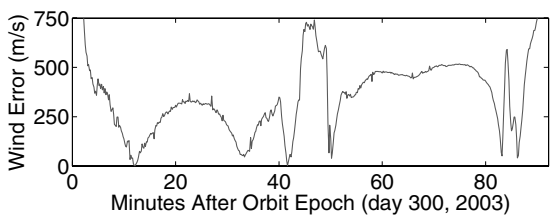

Fig. 3 Absolute error between wind calculations using two methods: 1) accounting for and removing lift and 2) neglecting lift; both use the dual-axis method.

B. Noise-Error Sources

1. Instrument Precision

Currently, the along-track accelerometer is believed to be at the 3×10^{-9} ms^{-2} level [12]. Figure 4 shows the amount of error in density caused by the precision of the accelerometer. During this orbit, the along-track accelerometer precision accounts for less than 0.93% error in density estimates, with a mean error of 0.47%.

Although the precision of the accelerometer does not play a large role in density errors, wind-speed estimates are quite sensitive to it. Wind-speed estimates require both along-track and cross-track accelerometer observations, which in turn increases the error. The cross-track accelerometer is also believed to be at the 3×10^{-9} ms^{-2} level [12]. Figure 5 shows the large effect of accelerometer precision on wind-speed errors. During this orbit, mean wind-speed errors are 26.0 and 15.4 ms^{-1} when using the single-axis and dual-axis methods, respectively.

2. Radiation Pressure

Figure 4 shows the amount of error in the density estimates caused by modeling SRP over a typical orbit. These error estimates assume an inaccuracy in our SRP model of 8%, which was calculated by comparing jumps in the measured acceleration with the modeled acceleration, when CHAMP is entering and exiting Earth's shadow (as described in Sec. II.C). During this period, CHAMP is in a near-noon/midnight local-time orbit, causing the along-track density error due to SRP to be at maximum levels. However, we see from Fig. 4 that SRP causes less than 0.54% of an error in the neutral density estimates. Because of the fact that the acceleration due to drag is

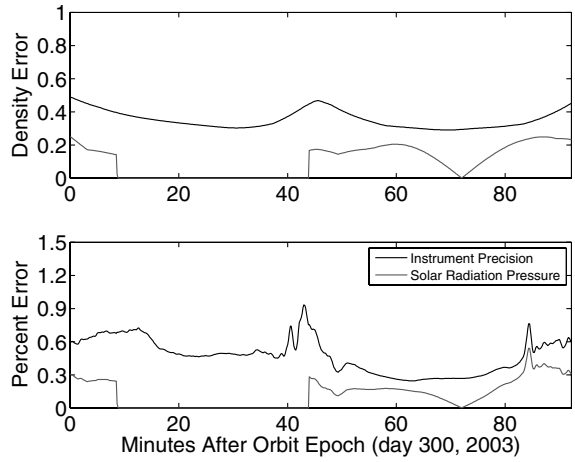

Fig. 4 Noise error (top, 10^{-13} kg/m^3) and percent error (bottom) in density estimates.

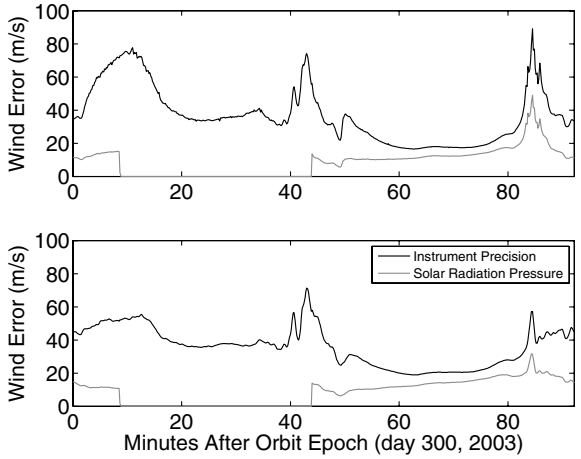

Fig. 5 Noise error in wind estimates when using the single-axis method (top) and the dual-axis method (bottom).

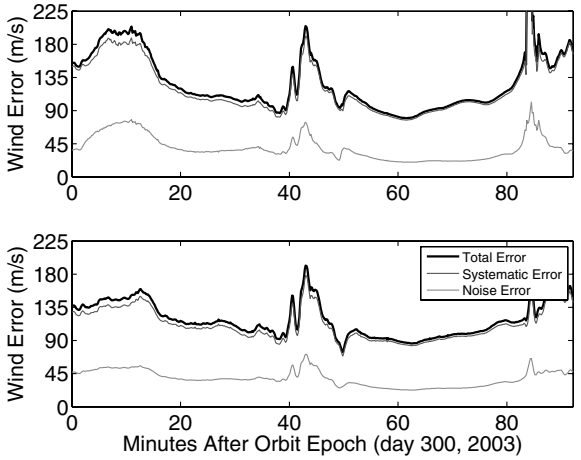

Fig. 7 Total error in wind estimates when using the single-axis method (top) and the dual-axis method (bottom).

much larger than the acceleration due to SRP, density errors caused by SRP rarely exceed 1% for the entire year of 2003.

Figure 5 shows the larger effect that errors in the SRP model have on cross-track wind-speed estimates using both solutions to Eq. (2). When the satellite moves into Earth's shadow, modeling of SRP is not needed and hence there is no SRP error; however, when sunlit, errors become as large as 49.0 and 31.6 ms^{-1} using the single-axis and dual-axis methods, respectively. On average, the errors caused by SRP are comparable for both solutions of the Eq. (2), however, the dual-axis method produces a lower maximum error. In either case, these errors contribute to just a fraction of the total errors during noon/midnight local-time sampling. It should be noted that errors will be at maximum levels when CHAMP is in the dawn/dusk local-time sector, at which time wind errors caused by SRP alone can exceed 80 ms^{-1}.

C. Total Error

1. Neutral Density

Combining the systematic and noise errors yields the total error, shown in Fig. 6 for density. During this orbit, the mean error in density is 8.5%, although at times it reaches as high as 15.6%. Overall, systematic errors contribute the most to the total density errors, with a mean of 8.4%. These errors can reach as high as 15.6%, due mostly to the neglected winds.

The relatively low amount of error encountered away from the poles (less than 10%) makes the neutral density data set a great asset to the thermosphere community for use in low- to midlatitude studies. In addition, the added advantage of the high spatial and temporal resolution outweigh the drawbacks of the error.

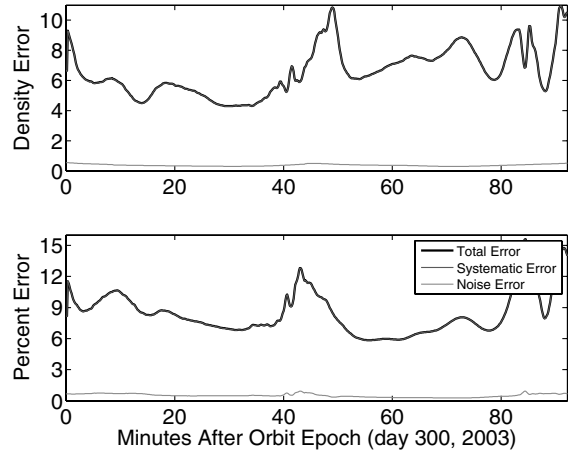

Fig. 6 Total error (top, 10^{-13} kg/m^3) and percent error (bottom) in density estimates.

2. Cross-Track Wind Speed

Figure 7 combines the systematic and noise error to show the total error in wind estimates. Mean total wind errors are 129.4 and 117.9 ms^{-1} when using the single-axis and dual-axis methods, respectively. Without an additional method to reduce this error, accurate estimates of cross-track wind speed are unattainable. Using either method, systematic errors, dominated by cross-track bias and scale factor errors, contribute the most to the total wind errors. Without the errors of the cross-track bias and scale factors, the total error would be on the order of 79.2 and 66.7 ms^{-1} when using the single-axis and dual-axis methods, respectively. Fortunately, over the course of a day, the effects of cross-track bias and scale factors are fairly constant. When these winds are interpreted as being the deviation from the cross-track wind speed at lower latitudes (i.e., below $\pm 10^{\circ}$), much of the error associated with the cross-track bias and scale factors is eliminated. However, this does introduce a large ambiguity into the estimates. One solution to this problem is the use of other thermosphere wind measurements as instrument calibration. Ground measurements could be used during a flyover by a satellite with an accelerometer, and data from other satellites could be used when their orbital planes are aligned. In theory, this option would greatly reduce the errors while retaining the advantages of the cross-track wind-speed database, such as the high temporal and spatial resolution. However, there are currently no thermosphere measurements suitable for this task.

Regardless of the large errors, the single-axis method was shown to be much more sensitive to both systematic and noise errors, with an average increase of 5–10% in total error. When combined with the fact that the dual-axis method produces more stable estimates of error (i.e., without any large spikes), the dual-axis method clearly operates much better than the single-axis method.

IV. Results

In this section, results are presented for two cases to illustrate some of the many applications of the CHAMP density and cross-track wind-speed data set. The first example is a comparison with model outputs. The semi-empirical horizontal wind model (HWM-93) and the self-consistent thermosphere–ionosphere electrodynamic general circulation model (TIEGCM) are used to show both similarities and differences when compared with the cross-track wind speeds derived from CHAMP. The second example compares CHAMP cross-track winds with estimates of ion drift speeds from the Defense Meteorological Satellite Program (DMSP-15).

A. Model Comparison

Atmospheric density models are most in error during geomagnetic storms, thus it is the response of the thermosphere during these storms that is of most interest. During the period spanning from late October to early November of 2003, an active region on the sun

(active region 486) produced flares and coronal mass ejections (CMEs) of intensities rarely seen before. This time period has been the subject of many thermosphere and ionosphere studies due to the extreme geomagnetic and flare activity that occurred [21,22]. It is our goal to compare CHAMP wind estimates with empirical models such as HWM-93 and self-consistent numerical models such as TIEGCM during periods of extreme geomagnetic activity to arrive at an understanding of the measurements in the context of the global response and to possibly ascertain any shortcomings inherent in either model.

The top panel of Fig. 8 shows cross-track wind estimates from CHAMP during the aforementioned storm period. The middle and bottom panels of Fig. 8 show the model output for TIEGCM and HWM-93, respectively. Both models were sampled on CHAMP's orbit in the direction of the cross-track axis, which aligns closely with the zonal direction at lower latitudes (less than 80°). To compensate for the bias offset in the CHAMP data caused by the estimation of cross-track bias and scale factors, each plot was offset. On a daily average, each plot agrees with a corotating atmosphere at low latitudes (less than $\pm 10°$).

The most noticeable trait of the wind data is the periodic effect at high latitudes, termed the "longitude-UT" effect, which is caused by the offset between geographic and geomagnetic poles. This trait is recreated quite well by both models. Aside from this effect, the CHAMP winds correspond very well with the TIEGCM model output at both high and low latitudes, with a mean absolute difference of 64.1 ms^{-1}. The correlation between the CHAMP data and the HWM-93 model output is not quite as strong, with a mean absolute difference of 73.1 ms^{-1}. Mainly, the HWM-93 model output does not exhibit the same quality of spatial resolution as the TIEGCM model and the CHAMP cross-track wind-speed estimates. However, large fluctuations in the HWM-93 model output corresponding to the CHAMP data can be seen early on days 302 and 303 and late on day 304 in the form of an eastward enhancement in both the daytime and nighttime winds.

B. Ion Velocity Comparison

To better understand the interactions between the driving forces and wind estimates, it is helpful to make comparisons with

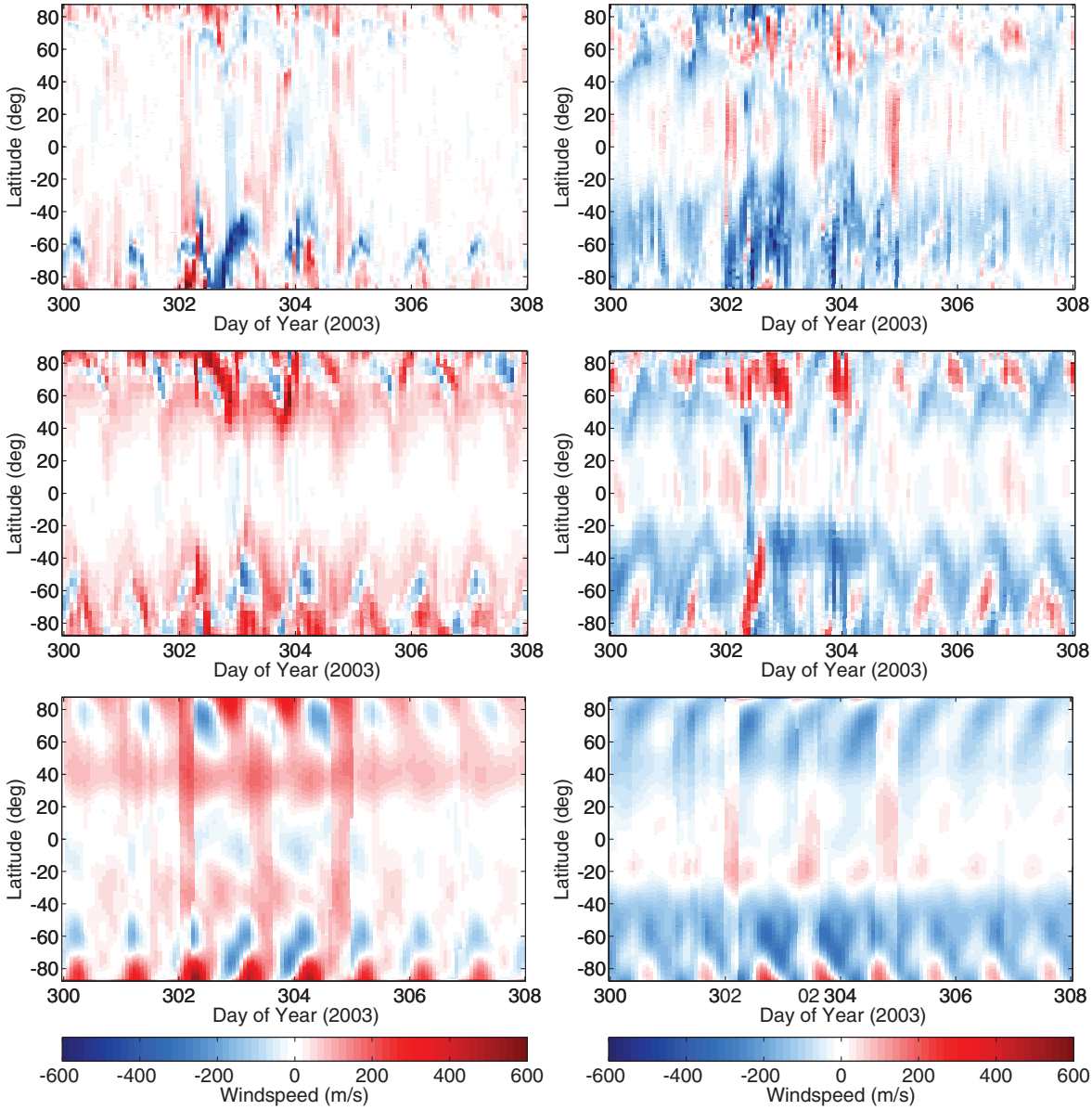

Fig. 8 CHAMP cross-track winds (top), TIEGCM horizontal winds sampled in the direction of the cross-track axis on the orbit of CHAMP (middle), and HWM-93 horizontal winds sampled in the direction of the cross-track axis on the orbit of CHAMP (bottom) during 27 October through 3 November 2003; daytime orbits (left, local time ~1320 hrs) and nighttime orbits (right, local time ~0120 hrs).

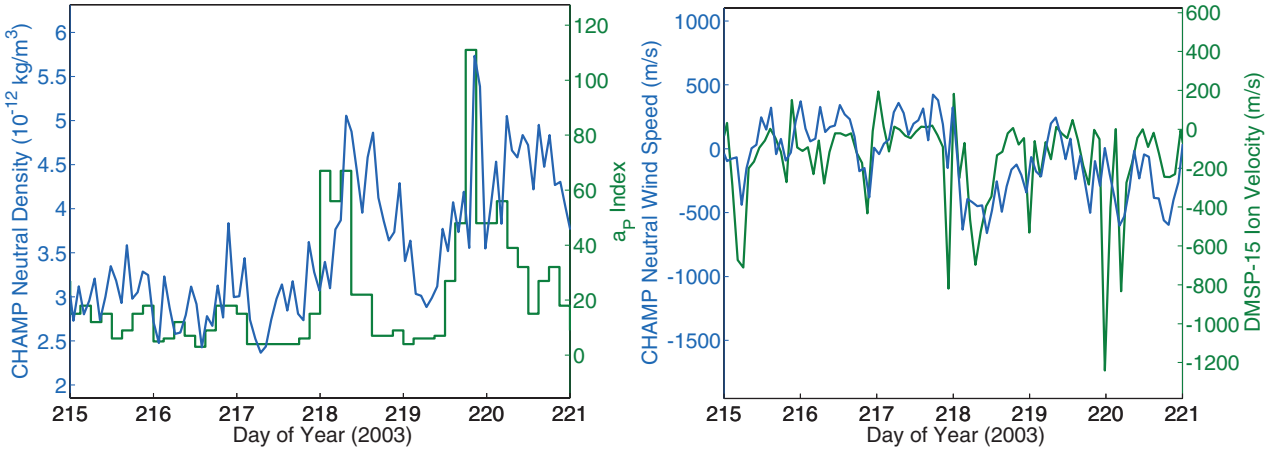

Fig. 9 CHAMP neutral density compared with the a_P index (left) and CHAMP winds compared with DMSP-15 cross-track ion velocity at 60° latitude and 2022 hrs local time (right).

measurements of ion velocity in the thermosphere. These measurements are made on the DMSP satellites. During a period spanning days 215–221, the local-time sampling of CHAMP aligned with the local-time sampling of the DMSP-15 satellite at 60° latitude. The DMSP satellites are in sun-synchronous orbits while CHAMP slowly precesses in local time, causing an alignment to occur every 133 days at a given latitude.

The left panel of Fig. 9 shows the correlation between CHAMP estimates of density and the a_P index provided by the National Geophysical Data Center (NGDC).[§] This is mainly shown to indicate when geomagnetic activity is high. The right panel of Fig. 9 shows cross-track winds from CHAMP and ion velocities from DMSP-15. In this plot, the scales were chosen to show the maximum amount of correlation between the two data sets. During times of increased geomagnetic activity, spikes in ion velocity can be seen to correlate very well with enhancements in CHAMP cross-track winds.

V. Conclusions

In the context of our treatment of errors, density estimates are accurate to better than 15%. However, enhanced winds during times of increased geomagnetic activity can cause the error to increase up to 30%. The largest sources of error in accelerometer density estimates are the coefficient of drag, unmodeled winds, and the estimates of bias and scale parameters. For wind estimates, the largest sources of error are instrument precision and the estimates of bias and scale parameters. At this time, it is impossible to obtain absolute estimates of wind with any degree of accuracy. However, due to the fact that the majority of the errors are fairly constant over the course of one day, analyzing the changes in winds, as seen in Sec. IV, can mitigate this error and reveal some of the possible applications.

Both of the wind-speed methods shown in this paper have advantages and disadvantages. To start with, the dual-axis method makes use of a substitution that greatly reduces the error caused by the coefficient of drag and the neglected atmospheric winds. The single-axis method also has the problem of producing large spikes in cross-track wind speed and error. Spikes in the latter are exacerbated by the linearization of the single-axis solution that is carried out to estimate the errors. In either case, these spikes do not occur when using the dual-axis method. When all of these issues are weighed, the dual-axis method yields better results and more reliable estimates of error.

This analysis of atmospheric density and wind estimates from the CHAMP/STAR accelerometer data has demonstrated their potential to become a tremendous value for atmospheric studies. With the anticipated launch of many more accelerometer missions, there is a great opportunity to study the characteristics of the thermosphere with unprecedented spatial and temporal resolutions.

[§]Data available online at http://www.ngdc.noaa.gov [retrieved 20 April 2006].

Appendix: Deviation of Wind Speed

In this section, we expand on the governing Eq. (2), repeated in Eq. (A1), to deduce an estimate of wind speed from measurements of acceleration:

$$\boldsymbol{a}_{\mathrm{dl}} = -\frac{\rho}{2m}\sum_{i=1}^{13}\left\{A_i C_{Di}[(\boldsymbol{v}_c - \boldsymbol{w}_c)\cdot\hat{n}_i](\boldsymbol{v}_c - \boldsymbol{w}_c) + A_i\frac{\cos\theta_i}{\sin\theta_i}C_{Li}[(\boldsymbol{v}_c - \boldsymbol{w}_c)\times\hat{n}_i]\times(\boldsymbol{v}_c - \boldsymbol{w}_c)\right\} \tag{A1}$$

In the preceding equation, the assumption $\boldsymbol{a}_{\mathrm{dl}} = \boldsymbol{a}_d + \boldsymbol{a}_l = \boldsymbol{a}_{\mathrm{obs}} - \boldsymbol{a}_{\mathrm{sr}} - \boldsymbol{a}_{\mathrm{ea}} - \boldsymbol{a}_{\mathrm{ir}}$ is made. Two methods are outlined in this Appendix. The single-axis method uses only the measurement of acceleration in the cross-track axis, whereas the dual-axis method makes use of the ratio of acceleration in the cross-track direction to acceleration in the along-track direction.

Single-Axis Method

Making use of the distributive law for dot and cross products, as well as the triple vector product [i.e., $(\boldsymbol{A}\times\boldsymbol{B})\times\boldsymbol{C} = (\boldsymbol{A}\cdot\boldsymbol{C})\boldsymbol{B} - (\boldsymbol{B}\cdot\boldsymbol{C})\boldsymbol{A}$], we are able to arrange the equation as follows:

$$\boldsymbol{a}_{\mathrm{dl}} = -\frac{\rho}{2m}\sum_{i=1}^{13}A_i\left\{\left(C_{Di} - \frac{\cos\theta_i}{\sin\theta_i}C_{Li}\right)[(\boldsymbol{v}_{\mathrm{c}}\cdot\hat{n}_i)\boldsymbol{v}_{\mathrm{c}} - (\boldsymbol{v}_{\mathrm{c}}\cdot\hat{n}_i)\boldsymbol{w}_c - (\boldsymbol{w}_c\cdot\hat{n}_i)\boldsymbol{v}_{\mathrm{c}} + (\boldsymbol{w}_c\cdot\hat{n}_i)\boldsymbol{w}_c] + \frac{\cos\theta_i}{\sin\theta_i}C_{Li}[(\boldsymbol{v}_{\mathrm{c}}\cdot\boldsymbol{v}_{\mathrm{c}})\hat{n}_i - 2(\boldsymbol{v}_{\mathrm{c}}\cdot\boldsymbol{w}_c)\hat{n}_i + (\boldsymbol{w}_c\cdot\boldsymbol{w}_c)\hat{n}_i]\right\} \tag{A2}$$

We can now expand the wind vector $\boldsymbol{w}_c$ and the unit normal $\hat{n}_i$ into their x, y, and z satellite-body-fixed components, as appropriate, facilitating the solution for wind speed in the cross-track direction (i.e., $w_{c,y}$):

$$\boldsymbol{a}_{\mathrm{dl}} = -\frac{\rho}{2m}\sum_{i=1}^{13}A_i\left\{\left(C_{Di} - \frac{\cos\theta_i}{\sin\theta_i}C_{Li}\right)[(\boldsymbol{v}_{\mathrm{c}}\cdot\hat{n}_i)\boldsymbol{v}_{\mathrm{c}} - (\boldsymbol{v}_{\mathrm{c}}\cdot\hat{n}_i)\boldsymbol{w}_c - (w_{c,x}n_{ix} + w_{c,y}n_{iy} + w_{c,z}n_{iz})\boldsymbol{v}_{\mathrm{c}} + (w_{c,x}n_{ix} + w_{c,y}n_{iy} + w_{c,z}n_{iz})\boldsymbol{w}_c] + \frac{\cos\theta_i}{\sin\theta_i}C_{Li}[(\boldsymbol{v}_{\mathrm{c}}\cdot\boldsymbol{v}_{\mathrm{c}})\hat{n}_i - 2(w_{c,x}v_x + w_{c,y}v_y + w_{c,z}v_z)\hat{n}_i + (w_{c,x}^2 + w_{c,y}^2 + w_{c,z}^2)\hat{n}_i]\right\} \tag{A3}$$

Equation (A3) can be broken down into x, y, and z satellite-body-fixed scalar components of acceleration. For the solution of

cross-track wind speed, we are interested in the y component. After collecting terms, the equation becomes

$$\begin{aligned} a_{\mathrm{dl},y} = &-\frac{\rho}{2m}\sum_{i=1}^{13} A_i \Bigg\{ \left(C_{Di} - \frac{\cos\theta_i}{\sin\theta_i} C_{Li} \right) [(\boldsymbol{v}_\mathrm{c} \cdot \hat{n}_i) v_y \\ &- (w_{c,x} n_{ix} + w_{c,z} n_{iz}) v_y] + \left(\frac{\cos\theta_i}{\sin\theta_i} C_{Li} \right) [(\boldsymbol{v}_\mathrm{c} \cdot \boldsymbol{v}_\mathrm{c}) n_{iy} \\ &- 2(w_{c,x} v_x + w_{c,z} v_z) n_{iy} + (w_{c,x}^2 + w_{c,z}^2) n_{iy}] \\ &+ \left[\left(C_{Di} - \frac{\cos\theta_i}{\sin\theta_i} C_{Li} \right) [-(\boldsymbol{v}_\mathrm{c} \cdot \hat{n}_i) - v_y n_{iy} \right. \\ &\left. + (w_{c,x} n_{ix} + w_{c,z} n_{iz})] - 2\left(\frac{\cos\theta_i}{\sin\theta_i} C_{Li} \right) v_y n_{iy} \right] w_{c,y} \\ &+ \left[\left(C_{Di} - \frac{\cos\theta_i}{\sin\theta_i} C_{Li} \right) n_{iy} + \left(\frac{\cos\theta_i}{\sin\theta_i} C_{Li} \right) n_{iy} \right] w_{c,y}^2 \Bigg\} \end{aligned} \tag{A4}$$

Equation (A3) can be solved for $w_{c,y}$ by noticing the quadratic relationship. The solution takes the following form:

$$\begin{aligned} k_{y1} = &\sum_{i=1}^{13} A_i \left[\left(C_{Di} - \frac{\cos\theta_i}{\sin\theta_i} C_{Li} \right) (\boldsymbol{v}_\mathrm{c} \cdot \hat{n}_i - w_{c,x} n_{ix} - w_{c,z} n_{iz}) v_y \right. \\ &\left. + \left(\frac{\cos\theta_i}{\sin\theta_i} C_{Li} \right) (\boldsymbol{v}_\mathrm{c} \cdot \boldsymbol{v}_\mathrm{c} - 2 w_{c,x} v_x - 2 w_{c,z} v_z + w_{c,x}^2 + w_{c,z}^2) n_{iy} \right] \\ &+ \frac{2m}{\rho} a_{\mathrm{dl},y} \end{aligned} \tag{A5a}$$

$$\begin{aligned} k_{y2} = &\sum_{i=1}^{13} A_i \left[\left(C_{Di} - \frac{\cos\theta_i}{\sin\theta_i} C_{Li} \right) (-\boldsymbol{v}_\mathrm{c} \cdot \hat{n}_i - v_y n_{iy} \right. \\ &\left. + w_{c,x} n_{ix} + w_{c,z} n_{iz}) - 2\left(\frac{\cos\theta_i}{\sin\theta_i} C_{Li} \right) v_y n_{iy} \right] \end{aligned} \tag{A5b}$$

$$k_{y3} = \sum_{i=1}^{13} A_i C_{Di} n_{iy} \tag{A5c}$$

$$0 = k_{y1} + k_{y2} w_{c,y} + k_{y3} w_{c,y}^2 \tag{A5d}$$

$$w_{c,y} = \frac{-k_{y2} \pm \sqrt{k_{y2}^2 - 4 k_{y3} k_{y1}}}{2 k_{y3}} \tag{A5e}$$

Dual-Axis Method

A second method can also be employed to deduce cross-track winds from a three-axis accelerometer. Assuming that one can properly account for and remove the lift forces on the satellite, Eq. (A1) simplifies to Eq. (A6):

$$\boldsymbol{a}_d = -\frac{\rho}{2m}\sum_{i=1}^{13} \{A_i C_{Di} [(\boldsymbol{v}_\mathrm{c} - \boldsymbol{w}_c) \cdot \hat{n}_i]\} (\boldsymbol{v}_\mathrm{c} - \boldsymbol{w}_c) \tag{A6}$$

In the preceding equation, the assumption $\boldsymbol{a}_d = \boldsymbol{a}_\mathrm{obs} - \boldsymbol{a}_\mathrm{sr} - \boldsymbol{a}_\mathrm{ea} - \boldsymbol{a}_\mathrm{ir} - \boldsymbol{a}_l$ is made, where $\boldsymbol{a}_l$ has now been modeled and subtracted from the observational data. After removing the acceleration due to lift, the remaining solution is identical to the solution given by Liu et al. [14]. Equation (A6) can be split into three scalar equations:

$$a_{\mathrm{drag},x} = -\frac{\rho}{2m}\sum_{i=1}^{13} \{A_i C_{Di} [(\boldsymbol{v}_\mathrm{c} - \boldsymbol{w}_c) \cdot \hat{n}_i]\} (v_x - w_{c,x}) \tag{A7a}$$

$$a_{\mathrm{drag},y} = -\frac{\rho}{2m}\sum_{i=1}^{13} \{A_i C_{Di} [(\boldsymbol{v}_\mathrm{c} - \boldsymbol{w}_c) \cdot \hat{n}_i]\} (v_y - w_{c,y}) \tag{A7b}$$

$$a_{\mathrm{drag},z} = -\frac{\rho}{2m}\sum_{i=1}^{13} \{A_i C_{Di} [(\boldsymbol{v}_\mathrm{c} - \boldsymbol{w}_c) \cdot \hat{n}_i]\} (v_z - w_{c,z}) \tag{A7c}$$

Using the equations for the x and y axes and making the correct substitution, we are left with an equation that can be solved for the cross-track wind:

$$a_{\mathrm{drag},y} = \frac{a_{\mathrm{drag},x}}{v_x - w_{c,x}} (v_y - w_{c,y}) \tag{A8a}$$

$$w_{c,y} = v_y - \frac{a_{\mathrm{drag},y}}{a_{\mathrm{drag},x}} (v_x - w_{c,x}) \tag{A8b}$$

Acknowledgments

This work was supported under National Science Foundation (NSF) grant ATM-0208482 as part of the National Space Weather Program and NASA grant NNG04GN20H as part of the Graduate Student Researchers Program. CHAMP is managed by the GeoForschungsZentrum Postdam (GFZ). The TIEGCM data were provided for our use by the National Center for Atmospheric Research (NCAR).

References

[1] Kamide, Y., McPherron, R. L., Gonzalez, W. D., Hamilton, D. C., Hudson, H. S., Joselyn, J. A., Kahler, S. W., Lyons, L. R., Lundstedt, H., and Szuszczewicz, E., "Magnetic Storms: Current Understanding and Outstanding Questions," *Magnetic Storms*, Geophysical Monograph Vol. 98, 1997, pp. 1–19.

[2] Fuller-Rowell, T. J., Codrescu, M. V., Fejer, B. G., Borer, W., Marcos, F., and Anderson, D. N., "Dynamics of the Low-Latitude Thermosphere: Quiet and Disturbed Conditions," *Journal of Atmospheric and Terrestrial Physics*, Vol. 59, Sept. 1997, pp. 1533–1540.

[3] Prölss, G. W., "Magnetic Storm Associated Perturbations of the Upper Atmosphere," *Magnetic Storms*, Geophysical Monograph Vol. 98, 1997, p. 227.

[4] Reigber, C., Lühr, H., and Schwintzer, P., "CHAMP Mission Status," *Advances in Space Research*, Vol. 30, No. 2, 2002, pp. 129–134.

[5] Tapley, B. D., Bettadpur, S., Watkins, M., and Reigber, C., "The Gravity Recovery and Climate Experiment: Mission Overview and Early Results," *Geophysical Research Letters*, Vol. 31, May 2004, pp. 9607–+.

[6] Readings, C. J., and Reynolds, M. L., *Gravity Field and Steady-State Ocean Circulation Mission*, edited by C. J. Readings and M. L. Reynolds, Nine Candidate Earth Explorer Missions, ESA, Paris, 1996.

[7] Ritter, P., and Lühr, H., "Estimation of Field-Aligned Currents with a multiSatellite Mission (Swarm)," *AGU Fall Meeting*, Abstract No. GP31A-0823, American Geophysical Union, Washington, D.C., Dec. 2004.

[8] Marcos, F. A., and Forbes, J. M., "Thermospheric Winds from the Satellite Electrostatic Triaxial Accelerometer System," *Journal of Geophysical Research*, Vol. 90, No. 9, July 1985, pp. 6543–6552.

[9] Jacchia, L. G., "Static Diffusion Models of the Upper Atmosphere with Empirical Temperature Profiles," *Smithsonian Contributions to Astrophysics*, Vol. 8, No. 9, 1965, p. 215.

[10] Hedin, A. E., Reber, C. A., Newton, G. P., Spencer, N. W., Brinton, H. C., Mayr, H. G., and Potter, W. E., "A Global Thermospheric Model Based on Mass Spectrometer and Incoherent Scatter Data MSIS, 2: Composition," *Journal of Geophysical Research*, Vol. 82, June 1977, pp. 2148–2156.

[11] Barlier, F., Berger, C., Falin, J. L., Kockarts, G., and Thuillier, G., "A Thermospheric Model Based on Satellite Drag Data," *Annales de*

Géophysique, Vol. 34, No. 1, 1978, pp. 9–24.

[12] Reigber, C., Balmino, G., Schwintzer, P., Biancale, R., Bode, A., Lemoine, J. M., König, R., Loyer, S., Neumayer, H., Marty, J. C., Barthelmes, F., Perosanz, F., and Zhu, S. Y., "A High-Quality Global Gravity Field Model from Champ GPS Tracking Data and Accelerometry (Eigen-1S)," *Geophysical Research Letters*, Vol. 29, July 2002, p. 37.

[13] Lühr, H., Grunwaldt, L., and Förste, C., "CHAMP Reference Systems, Transformations and Standards," GeoForschungsZentrum Potsdam (GFZ), TR RS-002, Potsdam, Germany, Apr. 2002.

[14] Liu, H., Lühr, H., Watanabe, S., Köhler, W., Henize, V., and Visser, P., "Zonal Winds in the Equatorial Upper Thermosphere: Decomposing the Solar Flux, Geomagnetic Activity, and Seasonal Dependencies," *Journal of Geophysical Research: Space Physics*, Vol. 111, July 2006.

[15] Luthcke, S. B., Marshall, J. A., Rowton, S. C., Rachlin, K. E., Cox, C. M., and Williamson, R. G., "Enhanced Radiative Force Modeling of the Tracking and Data Relay Satellites," *Journal of the Astronautical Sciences*, Vol. 45, No. 3, 1997, pp. 349–370.

[16] Knocke, P. C., Ries, J. C., and Tapley, B. D., "Earth Radiation Pressure Effects on Satellites," *AIAA/AAS Astrodynamics Conference*, AIAA, Washington, D.C., Aug. 1988, pp. 577–587.

[17] Bruinsma, S., and Biancale, R., "Total Densities Derived from Accelerometer Data," *Journal of Spacecraft and Rockets*, Vol. 40, No. 2, Apr. 2003, pp. 230–236.

[18] Cook, G. E., "Satellite Drag Coefficients," *Planetary and Space Science*, Vol. 13, Oct. 1965, pp. 929–946.

[19] Moe, K., Moe, M. M., and Wallace, S. D., "Improved Satellite Drag Coefficient Calculations from Orbital Measurements of Energy Accommodation," *Journal of Spacecraft and Rockets*, Vol. 35, No. 3, 1998, pp. 266–272.

[20] Beckwith, T. G., Marangoni, R. D., and Lienhard, J. H., *Mechanical Measurements*, Addison Wesley Longman, Reading, MA, 1993.

[21] Gopalswamy, N., Barbieri, L., Cliver, E. W., Lu, G., Plunkett, S. P., and Skoug, R. M., "Introduction to Violent Sun-Earth Connection Events of October–November 2003," *Journal of Geophysical Research: Space Physics*, Vol. 110, Sept. 2005, pp. 9–14.

[22] Gopalswamy, N., Barbieri, L., Lu, G., Plunkett, S. P., and Skoug, R. M., "Introduction to the Special Section: Violent Sun-Earth Connection Events of October–November 2003," *Geophysical Research Letters*, Vol. 32, Feb. 2005, pp. 3–5.

A. Ketsdever
Associate Editor